Application of surface-wave tomography to mineral exploration: a case study from Siilinjärvi, Finland.

Federico Da Col[1], Myrto Papadopoulou[1], Emilia Koivisto[2], Łukasz Sito[3], Mikko Savolainen[4], Laura Valentina Socco[1].

(1) Department of Land and Environmental Engineering, Politecnico di Torino, Torino Italy

(2) Department of Geosciences and Geography, University of Helsinki, Helsinki, Finland.

(3) Geopartner s.p. z.o.o, Krakow, Poland

(4) Yara Suomi Oy, Siilinjärvi, Finland

Corresponding author: Federico Da Col. Email: federico.dacol@polito.it

Keywords: Surface waves, Tomography, mining exploration

Abstract

In order to assess the feasibility and validity of surface-wave tomography as a tool for mineral exploration, we present an active seismic 3D case study from the Siilinjärvi mine in Eastern Finland. The aim of the survey is to identify the formation carrying the mineralization in an area south of the main pit, which will be mined in the future. Before acquiring the data, we performed an accurate survey design to maximize data coverage and minimize the time for deployment and recollection of the equipment. We extract path-averaged Rayleigh-wave phase-velocity dispersion curves by means of a two-station method. We invert them using a computationally efficient tomographic code which does not require the computation of phase-velocity maps and inverts directly for 1D S-wave velocity models. The retrieved velocities are in good agreement with the data from a borehole in the vicinity, and the pseudo-3D S-wave velocity volume allows us to identify the geological contact between the formation hosting most of the mineralization and the surrounding rock. We conclude that the proposed method is a valid tool, given the small amount of equipment used and the acceptable amount of time required to process the data.

Introduction

Surface-wave tomography is a well-established method in global and regional seismology (among many others, Ritzwoller and Levshin 1998; Shapiro et al. 2005; Yao, Beghein and Van Der Hilst 2008; Bensen, Ritzwoller and Shapiro 2008). It allows the mapping of the geological features of the crust and the upper mantle (e.g., Van Der Lee and Frederikssen 2005; Bensen et al. 2008; Lebedev and van

This article has been accepted for publication and undergone full peer review but has not been through the copyediting, typesetting, pagination and proofreading process, which may lead to differences between this version and the Version of Record. Please cite this article as doi: 10.1111/1365-2478.12903.

der Hilst 2008), but seismologists have also used shorter-period waves to map the shallow subsurface of smaller areas (e.g., Chourak et al. 2005; Mordret et al. 2011; Badal et al. 2013). An interesting approach is that of Orfanos et al. (2016), who applied surface-wave tomography to improve the initial model estimation for the local earthquake tomography, at the scale of a gas field, in a case where no prior information was available.

The method has also been applied at exploration-scale to both active and passive surveys. An example of application to active seismic data can be found in Socco et al. (2014). The authors showed how surface wave tomography is a valid alternative to classic multichannel analysis and applied it to a 2D dataset. An example of a 3D application can be found in Swoboda et al. (2013). The authors were able to detect old, land-filled mining facilities using surface waves generated by active sources and recorded by arrays of geophones approximately 1 km long. An example of exploration-scale application of surface-wave tomography to passive data is the work by Picozzi et al. (2009). The authors used seismic stations for a small-scale 2D passive survey and showed that the results of the tomography are in good agreement with those of previous radar and electrical-resistivity surveys.

The ability of surface-wave tomography to detect lateral variations in the subsurface also makes it attractive for mineral exploration, since mineralized bodies typically have different petrophysical properties compared to the surrounding rocks (Airo and Mertanen 2008; Malehmir et al. 2017). Furthermore, the high velocity of propagation of surface waves in the stiff rocks typical of mining sites, allows a penetration depth in the order of a few hundred meters to be reached even using standard exploration geophones. This, together with the rather time-effective processing workflow, also makes it economically viable.

A possible outcome of surface-wave analysis is the computation of static corrections (Mari 1984; Socco et al. 2010) for seismic reflection imaging, which is becoming increasingly popular for mineral exploration (Durrheim and Maccellari 1991; Adam et al. 1998; Eaton, Milkereit and Salisbury 2003; Koivisto et al. 2012; Malehmir et al. 2017). A processing workflow using a multichannel approach to compute static corrections had recently been outlined by Papadopoulou et al. (submitted, this issue). The results were encouraging, even though they faced the challenge of the very sharp lateral variations typical of the fractured bedrocks where the ore bodies lie. A tomographic approach could help overcome this issue.

Despite the attractiveness, very few case studies of surface-wave tomography applied to mineral exploration are present in the literature and they only make use of ambient seismic noise records. An example can be found in Hollis et al. (2018). The authors recorded ambient seismic noise with 90 seismic sensors for 30 days in the Coldwell Complex (Canada). They then performed a surface-wave tomography, managing to identify the main geological structures of the mineralized area until a depth of 1500 m. It has to be noted that these authors did not carry out a complete depth inversion, but they estimated the depth of the tomographic layers relating it to the wavelength. Using the same dataset, Sharma et al. (2018) stacked correlograms to obtain an average seismic section, from which they computed the f-k spectrum. They then pick the Rayleigh-wave phase-velocity dispersion curve and inverted it with a Monte Carlo inversion code to obtain a one-dimensional S-wave velocity profile.

An indirect application of surface-wave analysis to passive seismic data for mineral exploration can be found in Smith et al. (2013) and Scheib et al. (2016). In the former, the authors deployed seven seismometers, while in the latter they used a single 3C station. In both case studies, the authors recorded ambient seismic noise data for a few hours. Using Multi-Mode Spatial Autocorrelation (MMSPAC, Asten 2006), together with the Horizontal to Vertical Spectral Ratio (HVSR, Nakamura 1989), the authors produced S-wave velocity profiles to map the shallow sedimentary layers on top of the mineralized bedrock. However, no information was provided about the crystalline rock where the mineralization lies.

In this paper, we want to assess the feasibility and validity of surface-wave tomography for mineral exploration, applied to active seismic data. To do this, we propose an application to a dataset acquired in September-October 2018, in a forest south of the main pit of the Siilinjärvi mine in Finland. The area is of fundamental importance for future mining as it is known that the carbonatite-glimmerite formation carrying most of the mineralization extends to the South, in the forest, from the main pit. The aim of this survey is to detect the horizontal and vertical extension of this part of the mineralized ore body.

The area has already been subject to previous geophysical investigations. Malehmir et al. (2017) presented the results of a survey consisting of 2D active seismic lines and data from three boreholes in the area. These included geophysical downhole logs and laboratory analyses (density and P-wave velocity) of the extracted cores. We use this information to build the initial model for the tomographic inversion and validate our results.

Geological Setting

The Siilinjärvi phosphorus mine (a map showing the location can be seen in Figure 1), operating since 1979, is amongst the oldest alkaline carbonatite-glimmerite deposits in the world (O'Brien, Heilimo and Heino 2015; Tichomirowa et al. 2006). The mine consists of two open pits: the main one is called Sarkjärvi (maximum depth 250 m) and a satellite one is called Saarinen (maximum depth 60 m). The size of the ore body is known to be approximately 1 km wide and 15 km long, extending down to 800 m depth (Malehmir et al. 2017). The host rock is granite-gneiss (Kresten 1980), where the carbonatite-glimmerite complex intruded. These emplacements make approximately 50% of the whole rock volume in the ore deposit (Malehmir et al. 2017) and they are of the highest importance since they contain most of the apatite, the main ore mineral. Finally, in the carbonatite intrusion, subvertical diabase dykes are present.

Malehmir et al. (2017) analyzed borehole data and ran laboratory measurements to evaluate the physical properties of the rocks present at the site. These analyses showed that the P-wave velocity, as well as density values show strong variations. The conclusion was that fracturing is the most influential factor affecting wave velocities, while the rock type has less influence. However, they highlighted how the carbonatite-glimmerite formation is more prone to fracturing and overall shows a lower velocity compared to the host rock.

The well closest to our investigation area is R628. The full log can be seen in Malehmir et al. (2017, Figure 6); in Figure 2, we show the sonic (Figure 2a) and density logs (Figure 2b). The main feature of the logs is a sharp velocity and density increase at approximately 210 m hole depth, identifying the

contact zone between the carbonatite-glimmerite and the underlying granite-gneiss (host rock). Furthermore, a lower velocity and density zone between 160 and 210 m depth is visible, probably due to a highly fractured layer. In the density log, we observe a very sharp increase at around 215 m depth, corresponding to a contact to the diabase.

Data Acquisition

The full seismic array, shown in the georeferenced map in Figure 1b, consists of 578 10-Hz vertical geophones connected to wireless stations, which contain a GPS locator, a transmitting antenna and a analog-to-digital converter. In order to continuously transmit the data of each station to the central recording van, the wireless stations have to communicate with each other. To ensure this, two neighboring stations have to be at a maximum distance of 50 m from each other, which is the main constraint given by the equipment in use. Furthermore, in presence of obstacles (e.g., vegetation, as in the forest area explored in this survey), this distance has to be further reduced to approximately 40 m. The array was aimed at recording both ambient noise and the active data that are analyzed in this work contemporarily, hence it recorded continuously for 13 days during which period a set of shots were blasted. The data were recorded with a sampling rate of 2 ms.

The area covered by the dataset can be divided into three different zones, as labeled in Figure 1b).

i) Main pit. Inside the main open pit, for both practical and safety reasons, the receivers were installed along the mine roads in use at the time of the survey. Other receivers were placed along a road surrounding the pit. The main interest here is to map the depth extent of the mineralized body, any major structures affecting the stability of the open pit and the extension of the mineralized body towards the south.

ii) Gypsum pile. Gypsum is a by-product of the phosphoric-acid concentrator and is piled up in this 2x1 km area. Receivers were deployed along the road encompassing the pile, with the aim to map the continuation of the mineralized body beneath the gypsum pile and any shallow fractures in which the highly acid (pH < 2) water from the gypsum pile could infiltrate.

iii) Forest. This area is of fundamental importance for future mining, as it is known that the mineralized ore body extends in the forest and it will be mined in the next years. The area extends for 2 km in the N-S and 1 km in the E-W direction. A map showing a zoom of this area can be seen in Figure 1c). In this paper, we focus on this part of the array.

We performed an accurate survey design for this part of the dataset. Specifically, even though the array was recording continuously the ambient seismic noise, the receivers were deployed to make the best possible use of the shots being blasted for the active lines while recording. The deployment design was optimized for subsurface illumination but also had to account for logistical constraints. The main logistical challenge is the fact that the forest in which the receivers were deployed is rather thick at times with very uneven and slippery terrain, sometimes making it difficult and unsafe to walk in. Therefore, for safety reasons and for the effectiveness of the deployment and recollection of the equipment, most of the receivers were placed along or as close as possible to the paths in the forest and few receivers were located out of the path to guarantee optimal subsurface illumination given the position of the sources. More specifically, to make sure that the selected receiver locations

were optimal, we estimated the azimuthal illumination given by the shots to the array (polar histogram in Figure 3a) and the distribution of the length of all the available paths (histogram in Figure 3b). The paths are well distributed over all azimuths and the path length is well distributed around a maximum of 300 m.

While the array was recording, three active lines were acquired (red stars in Figure2b), which used 250 g of dynamite as sources, blasted in 3-m-deep boreholes every 20 m. Of these shots, we only consider the 103 shots along line SM2 and the first 50 shots along SM3, since those further away from the forest did not provide enough power to illuminate the array. Four additional calibration shots were blasted at the locations indicated by yellow stars in Figures 1b) and 1c). These had to be exploded in small holes dug with a shovel as it was impossible to use the drilling machine in the thick forest. The total number of shots we consider is therefore 157.

Surface -Wave Retrieval: Selection of the Receiver Pairs and the Two-Station Method

We implement a code to automatically detect groups of receivers in line with each source at every azimuthal angle, with a tolerance of 1 degree. This is essential for accurate phase retrieval in the two-station method (Bloch and Hales 1968) and it also allows to apply multichannel analysis to extract reference curves where the number of aligned receivers is sufficient. An example is shown in Figure 4a), which shows 9 receivers in line with the source, covering a good portion of the area. We use the phase-shift method (Park, Miller and Xia 1998), with which it is possible to process unevenly spaced receivers to pick a dispersion curve. This is representative of the expected dispersion trend over most of the array and can therefore be used as a reference to mitigate the ambiguity on which maximum to pick in the cross-multiplication matrix for all pairs of receivers considered.

For extracting the dispersion curves, we use the two-station method as implemented by Boiero (2009) following Yao, Van Der Hilst and De Hoop (2006). It consists of three steps: i) we select a source and a pair of receivers from those in line with the source at a certain azimuth; ii) for both receivers, we compute the group-velocity matrix as group velocity envelope frequency by frequency using a multiple Gaussian filter (Dziewonski, Bloch and Landisman 1969, Yao et al. 2006), and we pick the event with maximum amplitude and use it to time-window the traces as in Yao et al. (2006) with a cosine shoulder to enhance the event corresponding to the Rayleigh wave; iii) we compute the cross-multiplication matrix by cross-multiplying the two windowed traces frequency by frequency. To transform the cross-multiplication amplitude from time to phase-velocity, we use a 3-spline interpolator, as in Yao et al. (2006). We pick the dispersion curves as maxima on the cross-multiplication matrix. To do this, we select manually a zone on the matrix plot in which the maxima are automatically searched. To identify the zone that contains the right maximum to be picked on the matrix plot, we superimpose the reference dispersion curve previously extracted with multi-station processing (Figure 5d).

For the selection of receiver pairs, to maximize azimuthal coverage, we randomly select an azimuthal angle and find the receivers in line with a source at that angle. Then, among the aligned receivers, a random pair (i.e. a random distance between the two receivers) is selected to maximize the path length (i.e., wavelength) distribution. An example of processing for one of the trace pairs is shown in Figure 5. In Figure 5a) we show the selected source and all the receivers that are found to be in line

given a certain azimuth. For two receivers among those in line we show the traces in Figure 5b). In Figure 5c we show the group velocity matrix of the receiver closer to the shot, where a clear maximum is present with a velocity of around 1500 m/s in the frequency range of 5 Hz to 50 Hz. The cross-multiplication matrix is shown in Figure 5d) with the picked dispersion curve (black dots). Here the importance of having a reference curve (white dots) is evident, as it removes the ambiguity on which maximum to pick. When picking the dispersion curve in the cross-multiplication matrix, we neglect points relative to wavelengths exceeding the distance between the source and the closest receiver.

We manually select the matrix region for the automatic maxima picking for 433 dispersion curves. A plot of the curves is shown in Figures 6a) and 6b) in the frequency-phase-velocity and in the phase-velocity-wavelength domain respectively. The frequency band ranges from approximately 6 Hz to 50 Hz, even though many curves do not have data points above 30 Hz thus limiting the resolution of the shallow layers. The wavelength range extends from a minimum of 40 m to a maximum of 500 m (Figure 6b) thanks to the high velocities, which are consistent with the reference dispersion curve and with the information from the boreholes. Based on this, we can preliminarily estimate a penetration depth of approximately 250 m, corresponding to half of the maximum wavelength (Abbis 1981). In Figure 6c) we show a polar histogram of the azimuths of the paths. The azimuthal distribution appears to cover all azimuths and also the length of the paths shown in Figure 6d) appear well-distributed, with a peak between 200 and 300 m, but with several paths exceeding 400 m length. Note that a few of the curves show an irregular trend and appear to be affected by the presence of noise in the area coming from traffic, as well as a drilling machine operating in the forest. This is a common problem when performing surface-wave analysis in stiff sites (Papadopoulou et al. submitted). Given the very large number of available paths, we are nonetheless able to select those from which we could extract curves of a quality high enough to be inverted. We visually check each picked curve and we rejected those that presented unrealistic, abrupt changes in the phase-velocity or contained too few points (frequency band smaller than 7 Hz). A final remark regarding the picking is that higher modes did not appear with a multichannel, or with the two-station method. We therefore assume that what we picked is the fundamental mode.

In order to evaluate our coverage at different investigation depths, in Figure 7 we plot what we call tomographic pseudo slices (Da Col et al. 2019). These consist of plots of the paths available in a certain half-wavelength interval (i.e., investigation depth), coloring them with their path-averaged (in the plots, “apparent”) Rayleigh-wave phase-velocity. The rays are denser between half-wavelengths of 60 and 105 m, with very dense coverage until 180 m. At very long half-wavelengths (195 – 235 m) only the south-western part of the area has enough coverage and therefore the results at these depths in the rest of the area should be neglected.

Tomographic Inversion

The inversion code is described in Boiero (2009). It assumes surface-wave propagation along great-circle paths using asymptotic ray theory. Raytracing is performed using a 4^{th} order Runge-Kutta scheme, and it considers bent rays. This is of high importance for our case study where we expect sharp lateral variation in the S-wave velocity. The inversion result is a pseudo-3D shear-velocity model by means of 1D profiles beneath grid-points. These are estimated from the dispersion data

computed along the paths, using a damped weighted least-squares inversion. This allows the code to skip the building of phase-velocity maps and to invert directly for the 1D models, making it computationally more efficient. The code makes it possible to set horizontal and vertical constraints in the regularization matrix. Horizontally, the constrain consists in setting a maximum variation in S-wave velocity between a model and the four neighboring ones. Vertically, it sets the maximum vertical variation between two layers in S-wave velocity within each 1D model.

Based on the outcome of the tomographic pseudo-slices (Figure 7), we set the maximum depth (i.e. the starting depth of the half-space) at 270 m. We then perform several tests to find the number of layers and the thickness of each layer which give the minimum misfit and at the same time are able to detect the horizontal and lateral variations we are interested in. We conclude that this is achieved with a model of 5 laterally homogenous layers, plus the half-space below them, the properties of which are reported in Table 1. The layer properties are based on the logs presented in Malehmir et al. (2017), in particular of well R628, which is the closest to the area of interest. We take values from the density and sonic log, computing the S-wave velocity from the sonic log assuming a Poisson ratio of 0.25, which is a reasonable value for these types of rocks (Lanaro and Fredriksson 2005). In the inversion process, the only parameter being updated is the S-wave velocity, while the others remain fixed. We set up a regular grid of 1D models, with distance between model points of 44 m. This spacing proved to be the best compromise between computational cost and horizontal resolution. The regularization matrix is initialized setting as spatial constrain a maximum variation in S-wave velocity between neighboring points in the horizontal direction to be at most 100 m/s. This value is defined on the basis of tests carried out with and without regularization as suggested by Boiero (2009).

Checkerboard Test

To assess the ability of the data to resolve anomalies in the subsurface properties, we run a checkerboard test. Starting from the model described in Table 1, we perturb the S-wave velocity by 10% positively and negatively in rectangular patches in alternating order. In Figure 8a) and 8b) we show horizontal cross-sections of the two perturbation patterns used to perform the checkerboard test together with the receiver layout (red triangles). Specifically, each layer has an opposite perturbation pattern to the previous one, so that the horizontal cross-sections shown in Figures 8c),8e),8g) (relative to depths of 30 m, 150 m and 270 m, respectively) should reconstruct the pattern shown in Figure 8a). Those shown in Figures 8d) and 8f) (relative to depths of 90 m and 210 m, respectively) should reconstruct the pattern shown in Figure 8b). Black and white patches indicate negative and positive perturbation, respectively. The length of the diagonal of each patch forming the checkerboard is of 400 meters. The deepest layer reaches a depth of 270 m, corresponding to the maximum half-wavelength.

By raytracing on this volume along the same paths as in the picked experimental curves and taking the same frequency points, we obtain synthetic dispersion curves. We perform a tomography on these curves and compare the results with the "true" model. It should be noted that, since the checkerboard test is aimed at assessing the resolution achievable with the available data, we do not apply any regularization. On the other hand, when inverting the real data, several levels of regularization were tested to select the optimal one.

We show the results of the checkerboard test in Figure 8, where we plot the reconstructed models per each layer next to the "true" models. We see that the better-reconstructed layers are those at depths of 90 and 150 m, corresponding to the half-wavelength interval where the coverage is maximum, with still very good resolution at 210 m. As already stated, when commenting Figure 7a), the shallower layer (30m) has poor coverage, leading to an inaccurate reconstruction of the checkerboard map. 270 m seem to be a good estimate of our maximum penetration depth, since at that depth the patches can still be detected, even though not well resolved, in the South-Western part of the domain. This is consistent with the coverage shown in Figure 7h) and confirms that only this part of the domain should be considered when interpreting the inversion of the real data.

Inversion Results

In Figures 9 a), b), c), d) and e) we show plots of horizontal sections of the tomographic inversion at depths of 30 m, 90 m, 150 m, 210 m and 270 m, respectively, as indicated above each figure. Very sharp lateral variations can be noted in all layers, with the position of the high- and low- velocity patches appearing to be consistent along the vertical direction. The much lower velocities at 30 m depth are probably due to weathering. Consistently with what we assessed in the checkerboard test, the lateral variations are very well detected at depths from 90 m to 210 m, while at 30 m and 270 m depth we see a smearing of the anomalies. To assess the validity of our results, we compare the S-wave velocities as computed by the tomography and those derived from the sonic log from well R628. We compute the S-wave velocity from the P-wave velocity log assuming a Poisson ratio of 0.25, typical of granitic rocks (Lanaro and Fredriksson 2005) and plot the results in Figure 10a) (blue line). We overlap this with red dots and error bars, representing the average velocity and uncertainty of each layer obtained from the tomography. We associate to each average S-wave velocity the uncertainty σ_{layer} given by

$$\sigma_{layer} = \sqrt{\frac{\sum_{i=1}^{n} \sigma_i^2}{N}}, \qquad (2)$$

Where σ_i^2 is the variance of each point in the layer obtained from the posterior covariance operator (Tarantola and Valette 1982), and *N* is the number of points in the layer. From this plot, we conclude that both the trend and the values of the velocities are compatible. Furthermore, the inversion also detected the decrease in S-wave velocity between 180 m and 210 m depth, which Malehmir et al. (2017) associate to a fractured zone. Following the results of the core analysis performed by Malehmir et al. (2017), we associate the lateral S-wave velocity variations to the transition from host rock to carbonatite-glimmerites, which are more prone to fracturing and therefore show lower velocities than the granite-gneiss. Furthermore, we overlay our results at 90 m depth (i.e., the layer where the lateral variations are best resolved) with a geological model (provided by Yara Suomi Oy) based on surface geology mapping and exploration drilling, as shown in Figure 10b). Such overlay indicates that the position of the lower-velocity area is compatible with that of the carbonatite complex (shown in pink in the figure) and the contact with the surrounding higher velocity host rock is well detected. Furthermore, the higher velocity areas in the carbonatite complex match the position of known diabase dykes. It will be a matter of future research to investigate whether the additional high velocity areas we detect correspond to unmapped dykes. We show such overlay only for the layer at a depth of 90 m, since the velocity anomalies are vertically quite consistent.

In Figure 11 we show a plot of the distribution of the residuals R, computed for each point forming the dispersion curves as

$$R = v_{obs} - v_{syn} \quad , \tag{1}$$

where v_{obs} is the phase-velocity of the picked dispersion curve and v_{syn} is the phase-velocity output from the tomography. In Figures 11a) and 11b) we show the distribution of the residuals for an inversion run with and without spatial constraints (regularization), respectively. Since the regularization did not affect significantly either the standard deviation of the residuals, or their value, we qualitatively conclude that the regularization used is reasonable (Tarantola 2005; Boiero and Socco 2010). In fact, assuming Gaussian distribution, center and standard deviation of the constrained inversion are -2.4 m/s and 150 m/s, respectively, while for the unconstrained inversion we obtain -2 m/s and 172 m/s. We find the values of the center of the distribution to be negligible and the standard deviation to be low enough to say that, overall, the curves are well fitted. In Figure 11c) and 11d) we show two examples of curve fitting, relative to the constrained inversion. In Figure 11c) the picked curve shows a regular trend and the inversion code was therefore able to fit it very well. On the other hand, in Figure 11d) the picked curve is affected by noise and the misfit is large even though, overall, the inverted curves fit the trends of the curves well. The presence of curves like the former, explain the high misfit values shown by some of the points as in Figure 11a).

Conclusions

We presented a case study that confirms the feasibility and effectiveness of active surface-wave tomography for mineral exploration. We considered a dataset, acquired in an area to be mined in the future, consisting of seismic gathers recorded using a 2D array of 240 10-Hz geophones deployed following both logistical requirements and the need to maximize the illumination and the shots blasted for two seismic reflection lines in the same area. We implemented a code to find the receivers in line with each source at every azimuthal angle. This allowed the automatic identification of the couples of receivers to be used for estimating the average phase-velocity dispersion curves using the two-station method. As is often the case with stiff sites, the data were challenging and affected by noise. However, given the very large number of available paths, it was possible to pick more than 400 curves of sufficient quality to be inverted. We applied a computationally efficient tomographic inversion to these curves to extract an S-wave velocity volume extending in depth from 30 m to 270 m. The retrieved S-wave velocity values are compatible with those from a well log in the area. Furthermore, the main geological feature of the area, which is the horizontal contact between the host rock and the carbonatite complex was identified. Furthermore, the presence of diabase dykes known from previous geological investigations within the carbonatite complex was confirmed.

The penetration depth of 270 m is already a valuable result, but it could be further improved by using lower-frequency geophones and sources. Furthermore, we could reach deeper layers by processing the ambient noise data acquired with the same array which might contain lower frequencies.

The method has proved to give valid and geologically relevant results. Cost-wise, the fairly small amount of equipment necessary to acquire the data makes it very attractive and, with some automatization in the picking process, the time to process the dataset would become fairly short.

Considering all of these aspects, we conclude that active surface-wave tomography is a valuable tool for mineral exploration.

Acknowledgements

Smart Exploration has received funding from the European Union's Horizon 2020 research and innovation programme under grant agreement No. 775971.

We thank Yara Suomi Oy for their very kind hospitality and extremely effective organization carried out by Aleksi Salo, as well as others, which allowed us to safely acquire the data.

The data were acquired using combined seismic equipment of Uppsala University and Geopartner sp. z o.o., for which we are thankful.

Next to them, we thank everyone who participated in the survey, especially the Master and Ph.D. students whose work was vital during the field work.

We also thank Mohammadkarim Karimpour, for helping us pick the dispersion curves.

List of Figures

Figure 1 - a) Map of Finland showing the location of the site. b) Map of the survey area. Black dots indicate the receivers, the red stars indicate the shots of the active lines and calibration shots in the open pit, while the yellow stars indicate the four calibration blasts in the forest. We indicate with a white rectangle the area of focus of this paper. c) zoom of the area of interest. Plots b) and c) include edited material from the Ortophoto Database of the National Land Survey of Finland 06/2018..

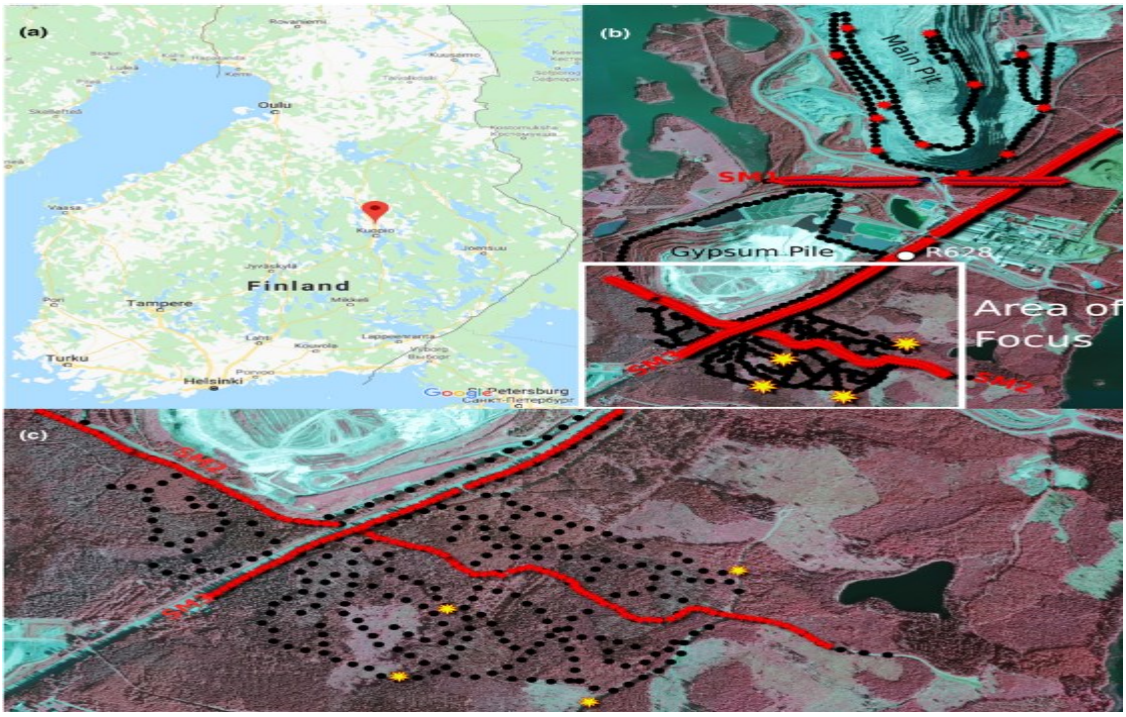

Figure 2 - Plots of the sonic (black) and density (red) log of well R628 (see Figure 1 for borehole location).

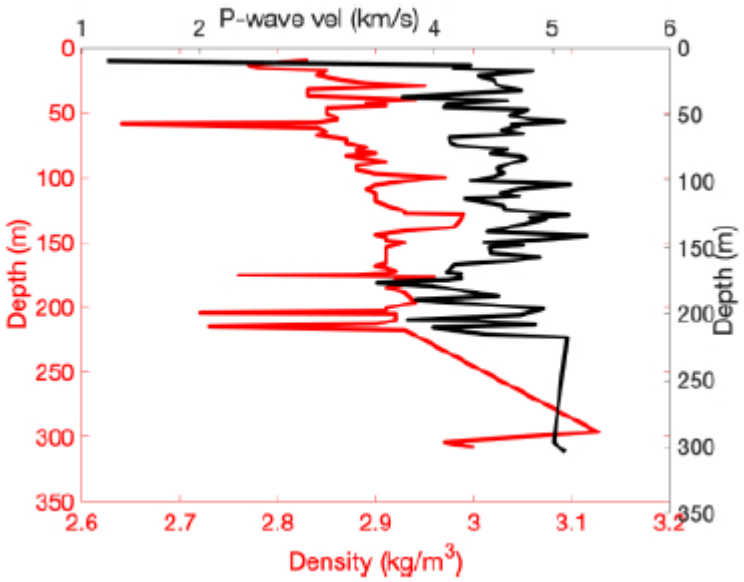

Figure 3 - Survey design. a) Polar histogram of the total azimuthal coverage given by all the used shots and the receivers in the forest. b) Histogram of the path length distribution.

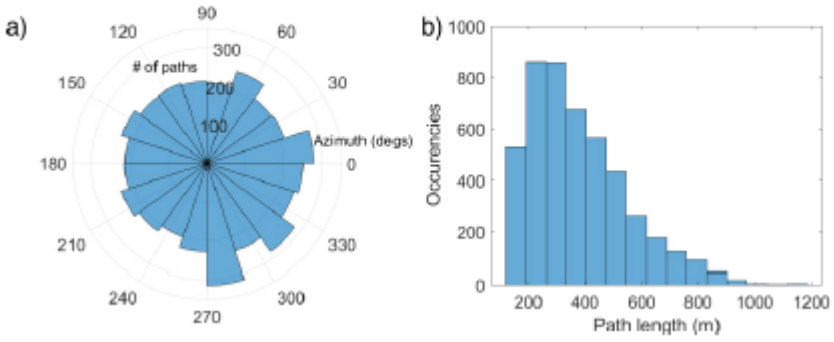

Figure 4 - a) Geometry of the receiver array, where we highlight the shot and 9 in-line receivers. b) Plot of the multichannel phase-dispersion image and picked reference dispersion curve.

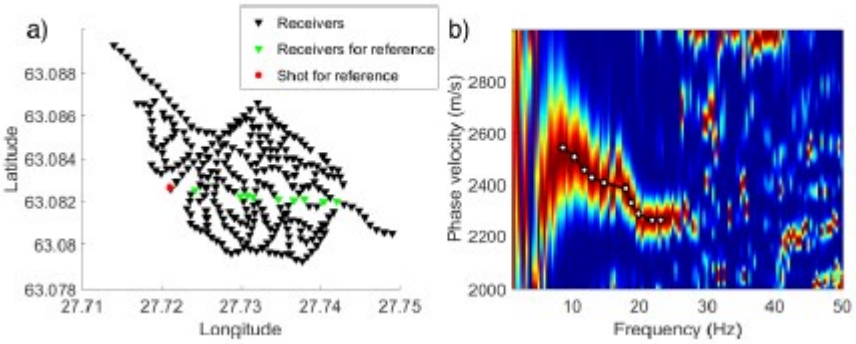

Figure 5 - a) Example of selection of receiver couples for two-station method: colored circles are receivers in line with the source indicated by the red star along azimuth 45 degrees. b) Wiggle plot of two selected traces (receivers indicated with + in a). c) Plot of the group-velocity matrix with clear maximum corresponding to the propagation mode of our interest. d) Plot of the phase-velocity matrix. Black and white dots represent the picked and reference curve, respectively.

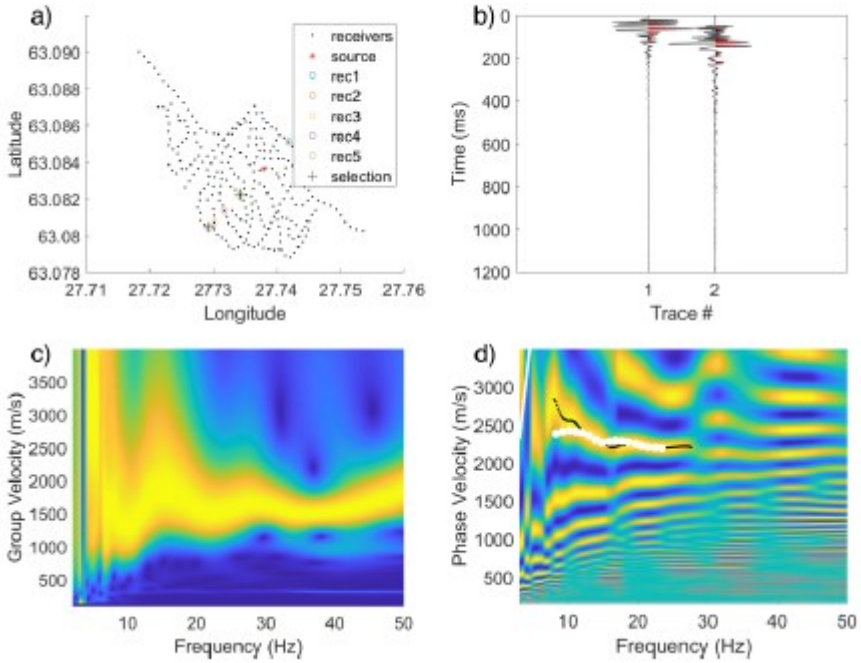

Figure 6 - Plot of the picked dispersion curves in a) frequency-phase-velocity domain, b) phase-velocity-wavelength domain. c) Polar histogram of the azimuthal coverage of the paths along which the curves have been picked. d) Histogram of the path length distribution of the picked curves

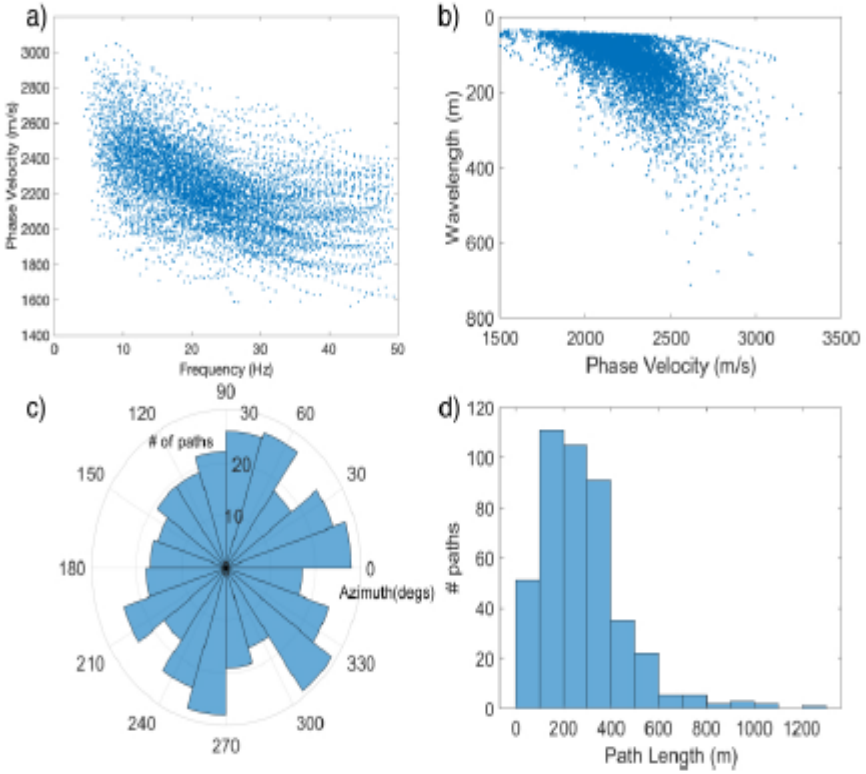

Figure 7 - Plots of tomographic pseudo-slices at several half- wavelength intervals. a) 10-40m, b) 30-50m, c) 60-90 m, d) 75-105m, e) 135-165m, f) 150-180m, g) 195-225m, h) 255-285m.

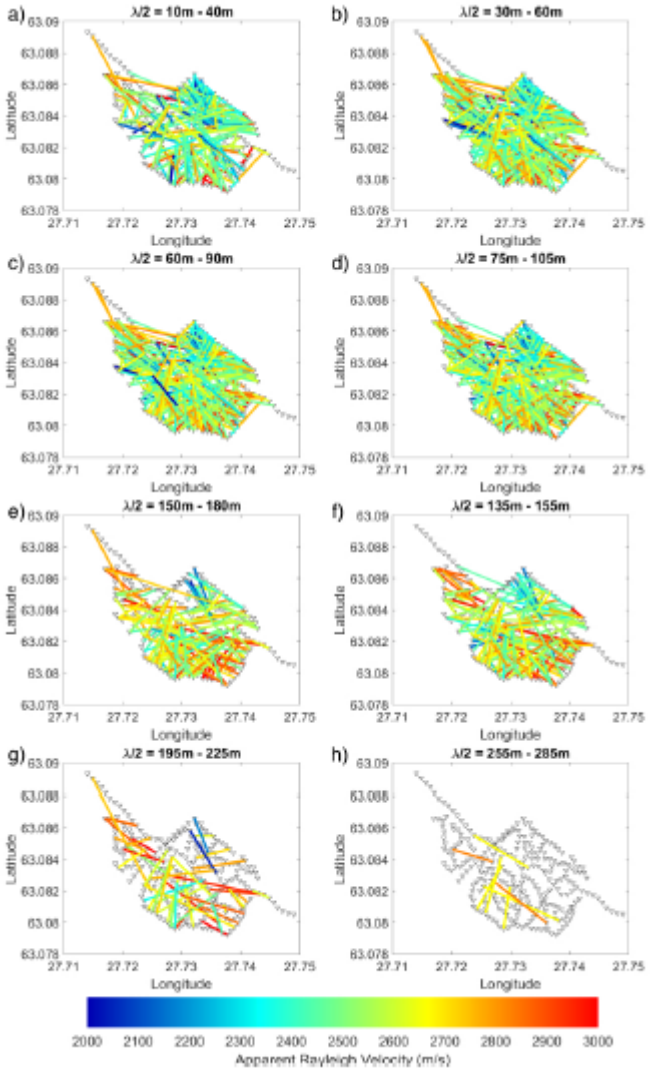

Figure 8 – a) Geometry of the checkerboard test. Red triangles indicate the receivers, Black and white squares indicate negative and positive perturbation, respectively. This perturbation pattern is relative to the layers at 30 m (c) 150 m (e) and 270 m (g). b) Geometry of the checkerboard test. This perturbation pattern is relative to the layers at 90 m (d) and 210 m (f). c), d), e), f) and g) show horizontal cross-sections of the checkerboard model as reconstructed by the tomographic inversion at depths of 30 m, 90 m, 150 m, 210 m, and 270 m, respectively.

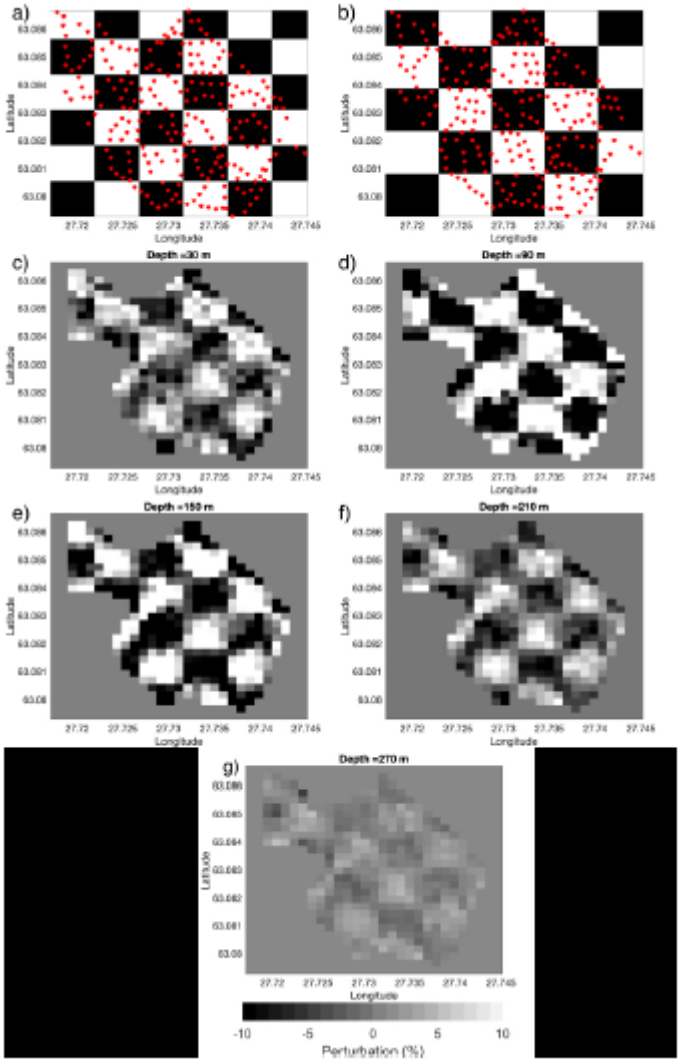

Figure 9 - Plots of horizontal sections of the 3D volume result of the tomography at depths a) 30 m, b) 90 m, c) 150 m, d) 210 m, e) 270 m, where we only show the model points where we have coverage at the necessary wavelengths, as shown in the pseudo slices (Figure 4h).

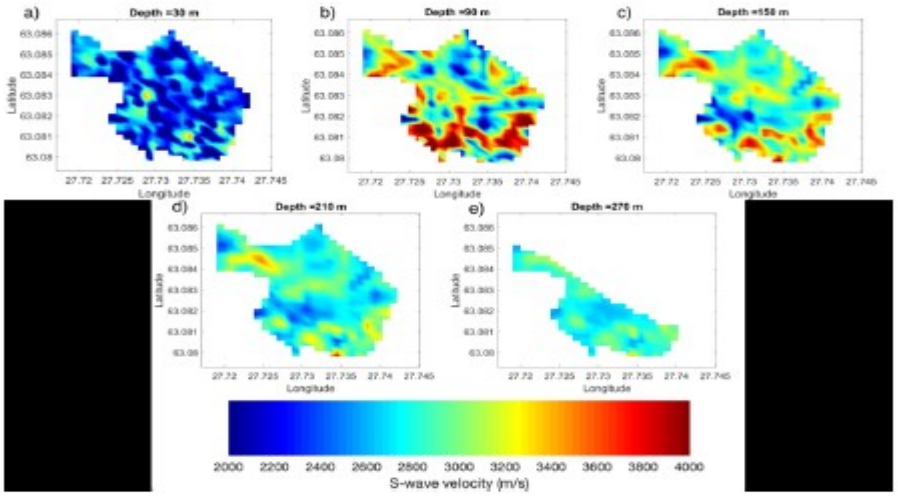

Figure 10 - a) S-wave velocities computed from the sonic log of well R628 assuming a Poisson ratio of 0.25 (blue line) and the average velocity and uncertainty obtained from the tomography (red data points with uncertainty). b) Overlay of the known geology of the area (provided by Yara Suomi Oy) with the S-wave velocity model output by our tomography at a depth of 90 m.

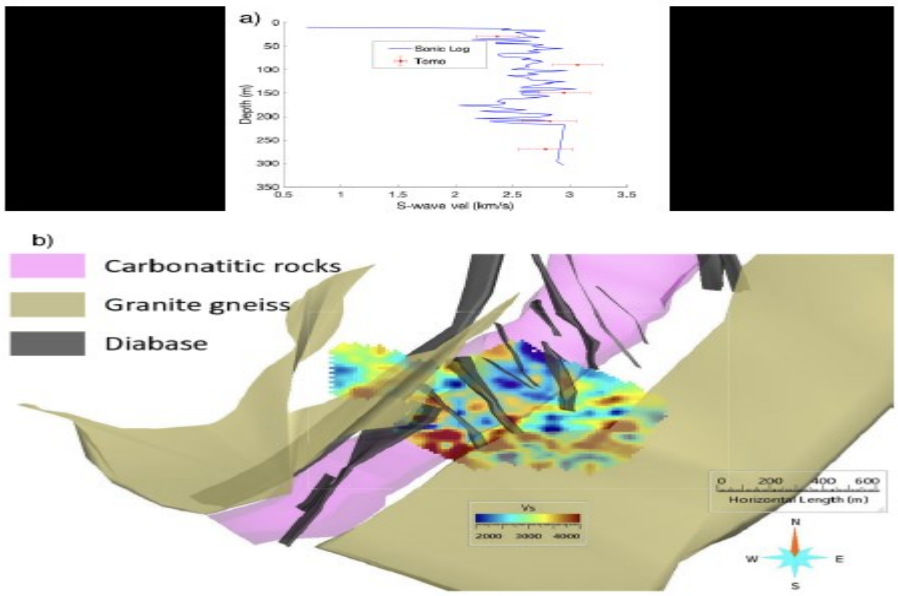

Figure 11 - Plot of the residual distribution for inversions run a) constrained (mean = -2.4 m/s, standard deviation = 172 m/s) and b) unconstrained (mean = -2 m/s, standard deviation = 150 m/s). c) Example of a typical fitting at the last iteration of the constrained inversion and d) fitting of a noisy curve, with large misfit.

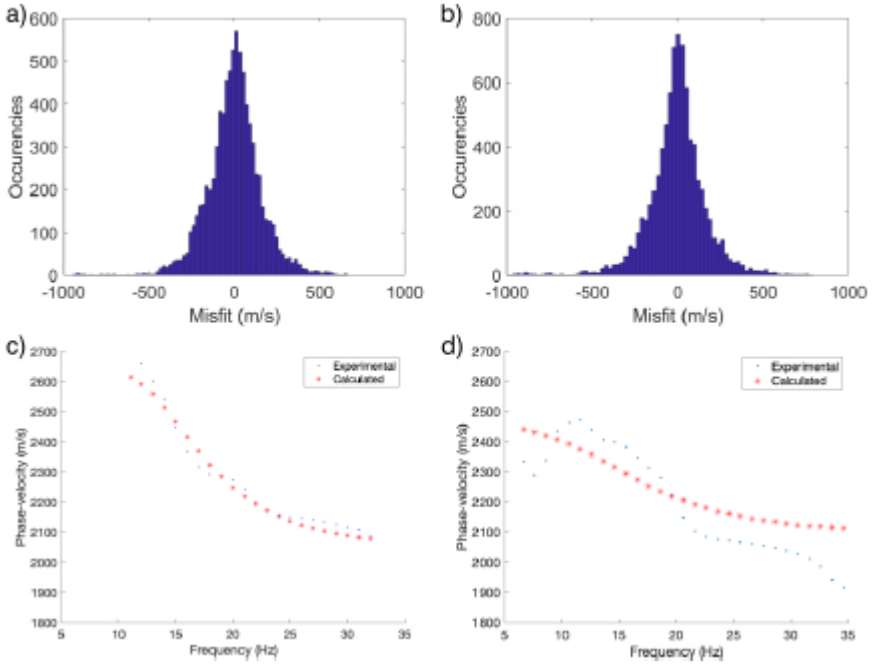

List of Tables

Table 1 - Properties of the initial model of the tomographic inversion. The same model has been perturbed by ±10% to perform the checkerboard test.

Layer n.	**1**	**2**	**3**	**4**	**5**	**Half-Space**
Thickness (m)	30	60	60	60	60	
Poisson	0.25	0.25	0.25	0.25	0.25	0.25
Density (km/m^3)	2.7	2.7	2.7	2.7	2.7	2.7
S-wave velocity (m/s)	2200	2300	2400	2600	2800	2900

References

Abbiss C. P. 1981. Shear wave measurements of the elasticity of the ground. *Geotechnique* ***31(1)***, 91-104.

Adam E., Milkereit B. and Mareschal M. 1998. Seismic reflection and borehole geophysical investigations in the Matagami mining camp. *Canadian Journal of Earth Sciences* ***35(6)***, 686-695.

Airo M. L. and Mertanen S. 2008. Magnetic signatures related to orogenic gold mineralization, Central Lapland Greenstone Belt, Finland. *Journal of Applied Geophysics*, ***64*****(1-2)**, 14-24.

Asten M. 2006. On bias and noise in passive seismic data from finite circular array data processed using SPAC methods*, Geophysics* ***71***, V153–V162

Badal J., Chen Y., Chourak M. and Stankiewicz, J. 2013. S-wave velocity images of the Dead Sea Basin provided by ambient seismic noise. *Journal of Asian Earth Sciences* ***75***, 26-35.

Bensen G. D., Ritzwoller M. H. and Shapiro N. M. 2008. Broadband ambient noise surface wave tomography across the United States. *Journal of Geophysical Research: Solid Earth*,***113*****(B5).**

Bloch S. and Hales A. L. 1968. New techniques for the determination of surface wave phase velocities. *Bulletin of the Seismological Society of America* ***58*****(3)**, 1021-1034.

Boiero D. 2009. Surface wave analysis for building shear wave velocity models. *Ph.D. Thesis.*

Boiero D. and Socco L. V. 2010. Retrieving lateral variations from surface wave dispersion curves. *Geophysical Prospecting* ***58*****(6)**, 977-996.

Chourak M., Corchete V., Badal J., Gómez and F. and Serón, J. 2005. Shallow seismic velocity structure of the Betic Cordillera (southern Spain) from modelling of Rayleigh wave dispersion. *Surveys in geophysics*, ***26*****(4)**, 481-504.

Da Col F., Karimpour M., Papadopoulou M., Socco L.V., Koivisto E., Salo A., Sito L., Malehmir. A. and Savolainen M. 2019. Surface Wave Analysis from Mineral Exploration: a 3D Example from Eastern Finland*, 81st EAGE Conference and Exhibition 2019.*

Durrheim R. J. and Maccelari, M. J. 1991. Seismic exploration for precious metals in the hard rock environment. *SEG Technical Program Expanded Abstracts 1991*, *159-162.*

Dziewonski A., Bloch S., Landisman M. 1969. A technique for the analysis of transient seismic signals. *Bulletin of the seismological Society of America* ***59*****(1)**, *427-444.*

Eaton D. W., Milkereit B. and Salisbury M. 2003. Seismic methods for deep mineral exploration: Mature technologies adapted to new targets. *The Leading Edge* ***22*****(6)**, 580-585.

Hollis D., McBride J., Good D., Arndt N., Brenguier F., Olivier G. 2018. Use of ambient noise surface wave tomography in mineral resource exploration and evaluation. *SEG Technical Program Expanded Abstracts 2018*, 1937-1940.

Kresten P. 1980. The Alnö complex: Tectonics of dyke emplacement. *Lithos* **13**, 153–158.

Koivisto E., Malehmir A., Heikkinen P., Heinonen S. and Kukkonen I. 2012. 2D reflection seismic investigations at the Kevitsa Ni-Cu-PGE deposit, northern Finland. *Geophysics* ***77*****(5)**, WC149-WC162.

Lanaro F. and Fredriksson A. 2005. Rock Mechanics Model-Summary of the primary data. Preliminary site description Forsmark area-version 1.2 (No. SKB-R--05-83). *Swedish Nuclear Fuel and Waste Management Co..*

Lebedev S. and Van Der Hilst R. D. 2008. Global upper-mantle tomography with the automated multimode inversion of surface and S-wave forms. *Geophysical Journal International* ***173*****(2)**, 505-518.

Malehmir A., Heinonen S., Dehghannejad M., Heino P., Maries G., Karell F. and Salo A. (2017). Landstreamer seismics and physical property measurements in the Siilinjärvi open-pit apatite (phosphate) mine, central Finland. *Geophysics* ***82*****(2)**, B29-B48.

Mari J. L. (1984). Estimation of static corrections for shear-wave profiling using the dispersion properties of Love waves. *Geophysics* ***49*****(8)**, 1169-1179.

Mordret A., Shapiro N. M., Singh S., Roux P. and Barkved O. I. 2011. Low frequency passive seismic tomography using Valhall LoFS. *Third EAGE Passive Seismic Workshop-Actively Passive 2011*.

Nakamura Y. 1989. A method for dynamic characteristics estimation of subsurface using microtremor on the ground surface*, Q. Rep. Railway Tech. Res. Inst.* ***30***, 25–30.

O'Brien H., Heilimo E., Heino P. 2015. The Archean Siilinjärvi carbonatite complex. *Mineral deposits of Finland*, 327-343. Elsevier.

Orfanos C., Leontarakis K., Lois A., Polychronopoulou K. and Martakis N. 2016. Automatic passive seismic data processing with no prior information: the contribution of Surface Wave Tomography. *First Break* ***34*****(7)**, 75-84.

Papadopoulou M., Da Col F., Mi B., Bäckström, E., Marsden, P., Brodic B., Malehmir A. and Socco L.V. 2019. Surface-wave analysis for static corrections in mineral exploration: a case study from central Sweden. Submitted (this issue).

Park C. B., Miller R. D. and Xia J. 1998. Imaging dispersion curves of surface waves on multi-channel record. *SEG Technical Program Expanded Abstracts 1998,* 1377-1380.

Picozzi M., Parolai S., Bindi D. and Strollo A. 2009. Characterization of shallow geology by high-frequency seismic noise tomography. *Geophysical Journal International* ***176*****(1)**, 164-174.

Ritzwoller M. H., Levshin A. L. 1998. Eurasian surface wave tomography: Group velocities. *Journal of Geophysical Research: Solid Earth* ***103*****(B3)**, 4839-4878.

Shapiro N.M., Campillo M., Stehly L. and Ritzwoller M.H. 2005. High resolution surface wave tomography from ambient seismic noise, *Science* ***307*****,** 1615–1618.

Sharma H., Molnar S., Hollis D. and McBride J. 2018. Application of ambient-noise analysis and velocity modeling in mineral exploration. *SEG Technical Program Expanded Abstracts 2018*, 3072-3076. .

Smith N. R. A., Reading A. M., Asten M. W. and Funk C. W. 2013. Constraining depth to basement for mineral exploration using microtremor: A demonstration study from remote inland Australia. *Geophysics* ***78*****(5)**, B227-B242.

Scheib A., Morris P., Murdie R. and Delle Piane C. 2016. A passive seismic approach to estimating the thickness of sedimentary cover on the Nullarbor Plain, Western Australia. *Australian Journal of Earth Sciences* ***63*****(5)**, 583-598.

Socco L. V., Boiero D., Foti S., Maraschini M., Piatti C., Bergamo P., Garofalo F., Pastori M. and Del Molino G. 2010. Surface wave analysis for S-wave static correction computation. *SEG Technical Program Expanded Abstracts 2010,* 1929-1933.

Socco L. V., Boiero D., Bergamo P., Garofalo F., Yao H., Hilst R. D. V. D. and Da Col F. 2014. Surface wave tomography to retrieve near surface velocity models. *SEG Technical Program Expanded Abstracts 2014.* 2013-2018.

Swoboda U., Uchtmann S., Limbrock K., Elsen R., Orlowsky D., Telenga K., Koschare A. and Wollnik F. 2013. Seismic and Geoelectric Investigation of Historical Mining Structures-A Case Study. *Near Surface Geoscience 2013-19th EAGE European Meeting of Environmental and Engineering Geophysics*.

Tarantola A. 2005. Inverse problem theory and methods for model parameter estimation, *Siam*, Philadelphia.

Tarantola A. and Valette B. 1982. Generalized non-linear inverse problems solved using the least squares criterion. *Reviews of Geophysics and Space Physics* **20,** 219--232.

Tichomirowa M., Grosche G., Götze J., Belyatsk B. V., Savva E. V., Keller J. and Todt W. 2006. The mineral isotope composition of two Precambrian carbonatite complexes from the Kola Alkaline Province–Alteration versus primary magmatic signatures. *Lithos* ***91*****(1-4)**, 229-249.

Van Der Lee S. and Frederiksen A. 2005. Surface wave tomography applied to the North American upper mantle. *Seismic Earth: Array Analysis of Broadband Seismograms* ***157***, 67-80.

Yao H., Van Der Hilst R. D. and De Hoop M. V. 2006. Surface-wave array tomography in SE Tibet from ambient seismic noise and two-station analysis—I. Phase velocity maps. *Geophysical Journal International* ***166*****(2)**, 732-744.

Yao H., Beghein C. and Van Der Hilst R. D. 2008. Surface wave array tomography in SE Tibet from ambient seismic noise and two-station analysis-II. Crustal and upper-mantle structure. *Geophysical Journal International* ***173*****(1)**, 205-219.